

University of Groningen

Surface alloying of high-vanadium high-speed steel on ductile iron using plasma transferred arc technique

Cao, H.T.; Dong , X.P.; Pan, Z.; Wu, X.W.; Huang, Q.W.; Pei, Y.T.

Published in:
Materials & design

DOI:
[10.1016/j.matdes.2016.03.114](https://doi.org/10.1016/j.matdes.2016.03.114)

IMPORTANT NOTE: You are advised to consult the publisher's version (publisher's PDF) if you wish to cite from it. Please check the document version below.

Document Version
Publisher's PDF, also known as Version of record

Publication date:
2016

[Link to publication in University of Groningen/UMCG research database](#)

Citation for published version (APA):

Cao, H. T., Dong , X. P., Pan, Z., Wu, X. W., Huang, Q. W., & Pei, Y. T. (2016). Surface alloying of high-vanadium high-speed steel on ductile iron using plasma transferred arc technique: Microstructure and wear properties. *Materials & design*, 100(2016), 223-234. <https://doi.org/10.1016/j.matdes.2016.03.114>

Copyright

Other than for strictly personal use, it is not permitted to download or to forward/distribute the text or part of it without the consent of the author(s) and/or copyright holder(s), unless the work is under an open content license (like Creative Commons).

The publication may also be distributed here under the terms of Article 25fa of the Dutch Copyright Act, indicated by the "Taverne" license. More information can be found on the University of Groningen website: <https://www.rug.nl/library/open-access/self-archiving-pure/taverne-amendment>.

Take-down policy

If you believe that this document breaches copyright please contact us providing details, and we will remove access to the work immediately and investigate your claim.

Downloaded from the University of Groningen/UMCG research database (Pure): <http://www.rug.nl/research/portal>. For technical reasons the number of authors shown on this cover page is limited to 10 maximum.



Surface alloying of high-vanadium high-speed steel on ductile iron using plasma transferred arc technique: Microstructure and wear properties



H.T. Cao ^{a,b}, X.P. Dong ^{a,*}, Z. Pan ^a, X.W. Wu ^a, Q.W. Huang ^a, Y.T. Pei ^{b,*}

^a State Key Laboratory of Materials Processing and Die & Mould Technology, School of Materials Science and Engineering, Huazhong University of Science and Technology, Wuhan 430074, China

^b Department of Advanced Production Engineering, Engineering and Technology Institute Groningen, Faculty of Mathematics and Natural Sciences, University of Groningen, Nijenborgh 4, 9747, AG, The Netherlands

ARTICLE INFO

Article history:

Received 3 November 2015

Received in revised form 21 March 2016

Accepted 22 March 2016

Available online 7 April 2016

Keywords:

Plasma transferred arc technique
Surface alloying
High-vanadium high-speed steel coating
Ductile iron
Microstructure
Wear properties

ABSTRACT

A high-vanadium high speed steel (HVHSS) alloying layer was synthesized from pre-placed powders (V-Cr-Ti-Mo) on ductile iron (DI) substrate using plasma transferred arc (PTA) technique. The PTA-alloyed layer, characterized by microhardness, optical microscopy, XRD, EDS enabled SEM, TEM and pin-on-disk tribometry, consists of three main regions: top alloyed zone (TAZ), intermediate remelted zone (IRZ), and heat affected zone (HAZ) of the DI substrate. A large number of globular carbides particles with size smaller than 5 μm form in the TAZ through in-situ reactions between the alloying elements and graphite in the molten pool. Further microstructural characterizations indicate that the carbides are primarily vanadium carbide (VC), confirming the formation of the HVHSS layer. The maximum microhardness of the PTA-alloyed sample occurring at the subsurface is 950 HV_{0.2} which is 5 times that of the substrate. The HVHSS layer exhibits superior tribological performance in comparison to PTA-remelted DI, Mn13 steel and DI substrate. The enhanced performance is attributed to the formation of mixed hard-phases such as MC, M₇C₃, M₂₃C₆, martensite and grain refining through rapid solidification accompanying the PTA process.

© 2016 Elsevier Ltd. All rights reserved.

1. Introduction

Ductile iron (DI) is widely used in a broad range of industrial applications such as machine tool beds, cams, valves, cylinder blocks, etc., due to its low production cost combined with favorable properties like machinability, excellent castability and comprehensive strength-toughness [1–3]. However, in severe service circumstances like those in mining and rolling sectors, the low hardness and poor wear resistance limit its further industrial applications. Moreover, bulk or conventional surface treatment like flame surface hardening is ineffective to strengthen ferrite-matrix ductile iron since there is insufficient pearlite that can be transformed into martensite [4]. Recently, hardfacings introduced by melting and alloying via high-energy beams (e.g. laser beam, electron beam) are new trends in surface strengthening of ductile iron [5–7]. Rapid solidification and self-quenching during desired local surface remelting result in metastable phases which further transform into cementite, ledeburite and martensite, forming a similar structure with the hardened white cast iron [8–10]. However, the low-hardness cementite dominates in the white cast iron with a blocky or continuously interdendritic network morphology, elucidating its role as stress concentrator favoring matrix cracking. Therefore surface alloying is

considered as a more viable alternative because during the surface alloying process, the alloying powders dissolve into a melting pool to form hard, fine alloy-carbides acting as reinforcements to achieve favorable mechanical properties such as high hardness and good abrasion resistance [11].

High-speed steel (HSS) coating could be an ideal candidate for providing highly desired properties on a DI substrate because the HSS contains a variety of primary carbides rich in vanadium, chromium, tungsten and molybdenum, etc., which exhibits excellent comprehensive mechanical properties, highlighting its high resistance to wear, reliable toughness and hot hardness even at elevated temperatures [12–16]. For instance, Bourithis and Papadimitriou synthesized a M-type HSS coating on the surface of a plain steel by PTA technique [13]. However, the carbides were mainly a network of fishbone-shaped M₆C-type and plate-like M₂C-type carbides [17] that unfavorably grew around the grain boundaries instead of dispersive metal carbides (MC). V. Lazić et al. pointed out that carbides precipitated at the grain boundaries or arranged in a line significantly decrease resistance to

Table 1
Chemical composition of the ductile iron substrate (wt.%).

C	Si	S	Mn	P	Fe
3.7	2.7	0.03	0.3	0.04	Bal.

* Corresponding authors.

E-mail addresses: dongxp@mail.hust.edu.cn (X.P. Dong), y.pei@rug.nl (Y.T. Pei).

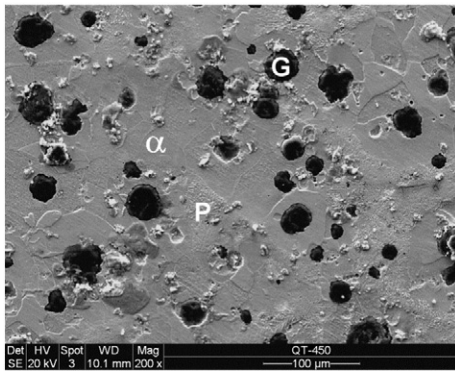


Fig. 1. SEM image of as-received DI, α: ferrite, G: graphite and P: pearlite.

Table 2
Chemical composition of the alloy powder (wt.%).

Element	V	Cr	Ti	Mo
Weight ratio	10	4	3	3

wear [18]. In general, alloy carbides provide higher hardness than cementite and martensite and hence greater resistance to wear. However, one should also note that the resistance to wear of carbides reinforced composites is not only determined by the hardness of carbides, but

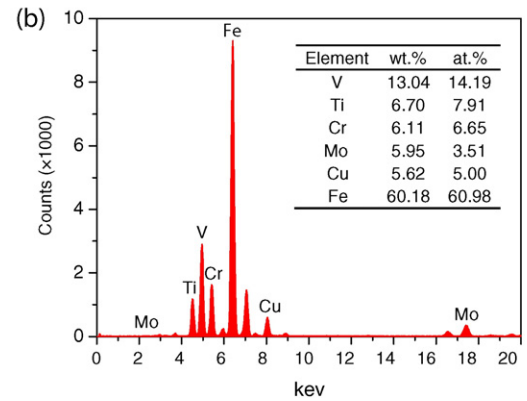


Fig. 3. (a) OM macroview and (b) XRF spectrum of the PTA-alloyed sample showing the alloying elements.

also by their size, distribution and shape. Large and irregularly-shaped carbides may be easily pulled out of the metal matrix or trigger stress fracture during the sliding tests [19]. Recently an as-cast high carbon

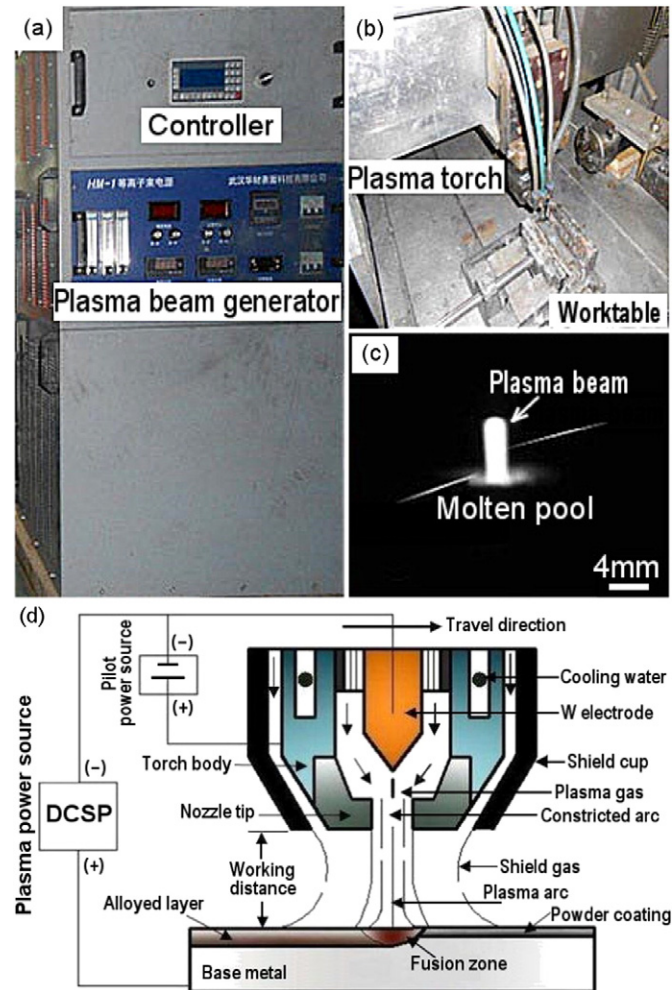


Fig. 2. PTA apparatus for surface alloying: (a) plasma generator, (b) plasma torch, (c) plasma beam and (d) diagram of the plasma torch [3].

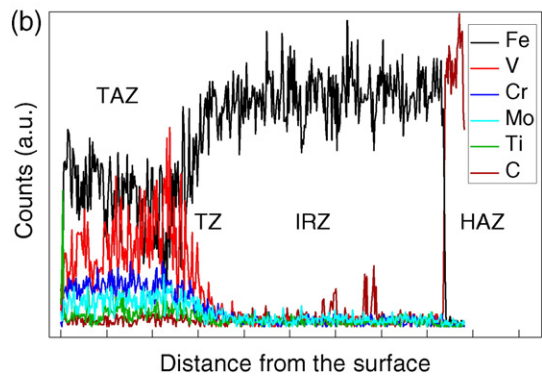
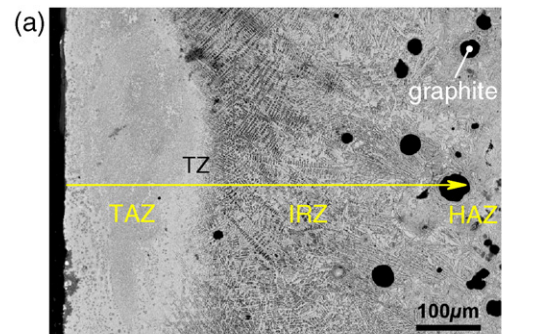


Fig. 4. (a) Cross-sectional overview of PTA-alloyed HVHSS layer on DI substrate showing three distinct zones: the top alloyed zone (TAZ), the intermediate remelted zone (IRZ) and the heat affected zone (HAZ); (b) EDS linear scan showing the element distribution along the depth direction as indicated by the arrow in panel (a).

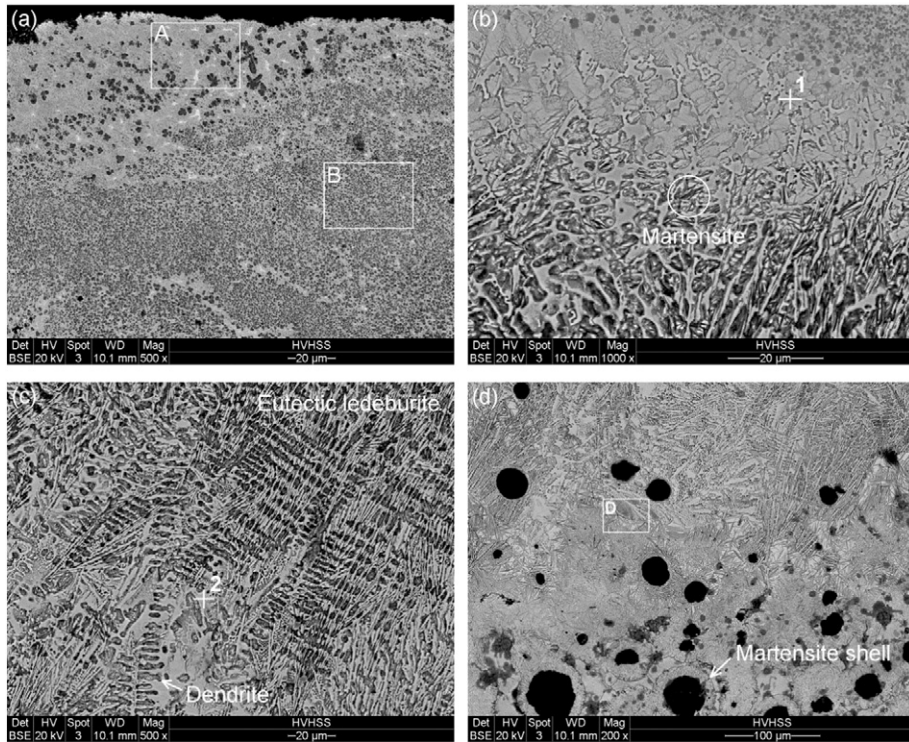


Fig. 5. Microstructural evolution: (a) the top alloyed zone (TAZ); (b) the transition zone (TZ) between TAZ and IRZ; (c) the intermediate remelted zone (IRZ); (d) the heat affected zone (HAZ).

high vanadium high speed steel (HVHSS) produced via traditional induction melting furnace has been extensively investigated by Wei et al [20–23]. The addition of 9–10 wt.% vanadium and 3–3.4 wt.% carbon in this newly developed HSS is intended to predominantly facilitate

the formation of fine and globular vanadium carbide (VC) particles, which could maximize the wear resistance by a combined effect of abrasive wear and impact toughness. Essentially, the high carbon high-vanadium high speed steel still belongs to the scope of white iron due

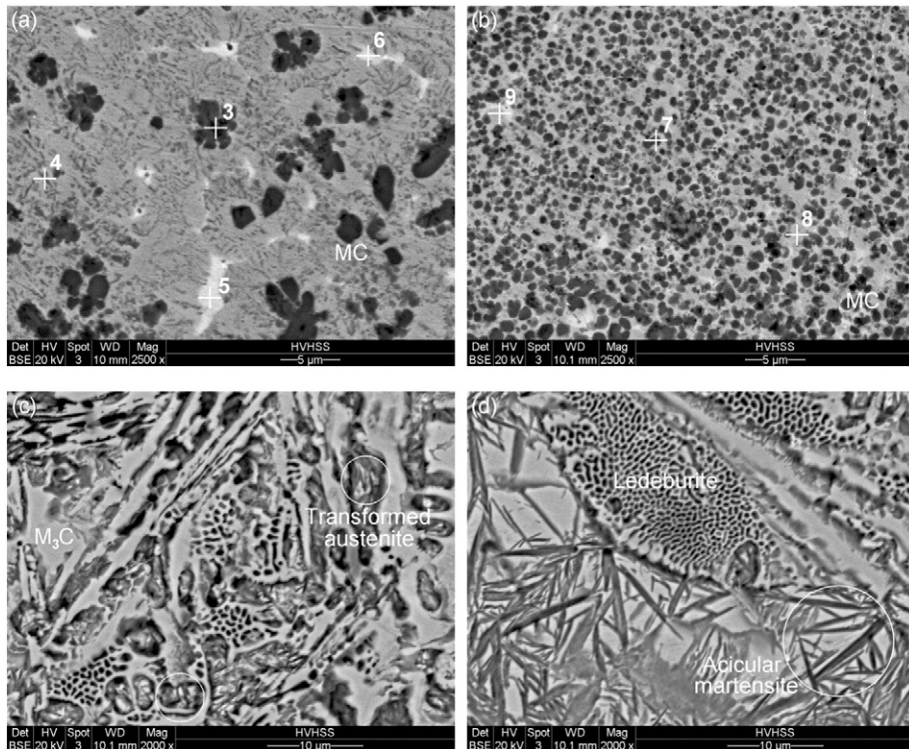


Fig. 6. (a) High magnification view of the area A in Fig. 5(a) in the upper TAZ; (b) high magnification view of the area B in Fig. 5(a) in the middle TAZ; (c) high magnification view of the IRZ; (d) high magnification view of the area D in Fig. 5(d) at the bottom of the IRZ close to the HAZ.

Table 3
EDS analysis of PTA-modified layer (at.%).

Element	Tested spot								
	1	2	3	4	5	6	7	8	9
V	2.42	–	20.42	11.96	9.76	0.67	21.87	13.69	8.33
Cr	2.89	–	4.23	6.69	8.30	0.29	5.24	6.20	9.66
Ti	0.29	–	3.24	0.39	0.27	1.59	1.33	1.21	0.11
Mo	0.61	–	2.76	2.82	3.32	0.43	3.44	2.39	6.51
Fe	60.94	71.89	36.60	56.24	62.94	8.85	32.37	53.61	56.80
C	32.85	28.11	32.76	21.91	15.04	88.17	35.76	22.90	18.59

to the high content of carbon, so it is reasonable and feasible to think of alloying a HVHSS layer on a DI substrate through the in-situ reactions between the strong carbide-forming elements (particularly vanadium) with the graphite from the DI. Notably, graphite is undesirable in terms of wear resistance because soft graphite phase interrupts the continuity of the hardened layer and acts as a potential source of crack nucleation [24,25].

Plasma beam has a number of remarkable advantages in surface modification compared with laser and electron beam processes due to its good surface quality, release of pre-treatment or vacuum environment, high energy efficiency and competitive running costs [11, 26–28]. In the present study, a plasma transferred arc (PTA) was employed to fabricate hard HVHSS layer on ductile iron substrates, achieving a HVHSS–white iron–ductile iron graded structure that exhibits good toughness, high hardness and wear resistance. The microstructure evolution, hardness and wear properties were preliminarily studied. Meanwhile, some prior results of PTA surface remelting are also presented for comparisons [3].

2. Experimental procedures

The chemical composition of the DI substrate is listed in Table 1. Fig. 1 presents the typical microstructure of the DI (QT-450) substrate consisting of spheroidal graphite nodules, ferrite and a small fraction of island-like pearlite. The diameter of the graphite nodules is in the range of 20–80 μm and the average hardness of the substrate is approximately 200 $\text{HV}_{0.2}$. The dimensions of the substrate specimens were 100 mm \times 50 mm \times 20 mm. Before PTA treatment, the surface of the substrates was ground thoroughly by 400-grit abrasive paper and then cleansed with acetone to remove oxides and contaminants.

The main chemical composition of the powder (all purities $\geq 99.0\%$) is given in Table 2. It is noteworthy that ferrovanadium (FeV_{50}) rather than pure vanadium was used because the latter is not merely active but expensive. The raw powder of 45–75 μm in size was mechanically blended in a planetary ball mill for 35 h to reduce its average diameter to be $< 5 \mu\text{m}$. The milling process was interrupted for 30 min every 4.5 h to avoid overheating and to invert the direction of rotation to promote homogenization. Afterwards, the powder mixed with some organic binders was smeared onto the DI substrate to form a pre-placed layer with a thickness of about 25 μm and then dried in a furnace for 30 min at the temperature of 150 $^{\circ}\text{C}$.

Fig. 2 shows the plasma apparatus and the schematic diagram of the plasma torch. This upgraded plasma torch could provide much higher energy density after a series of mechanical compression (narrowing the torch size) and thermal compression (water cooling) than conventional plasma arc. It was estimated that the maximum energy density could reach as high as 10^6 W/cm^2 . Several trials were conducted to optimize the final processing parameters: transferred arc current 70–100 A, scanning speed 0.9–1.6 m/min, spot diameter of plasma 4 mm, argon flux 2.5 L/min and an overlapping rate of 25% between tracks. Argon was also used as shielding gas to prevent oxidation of the PTA

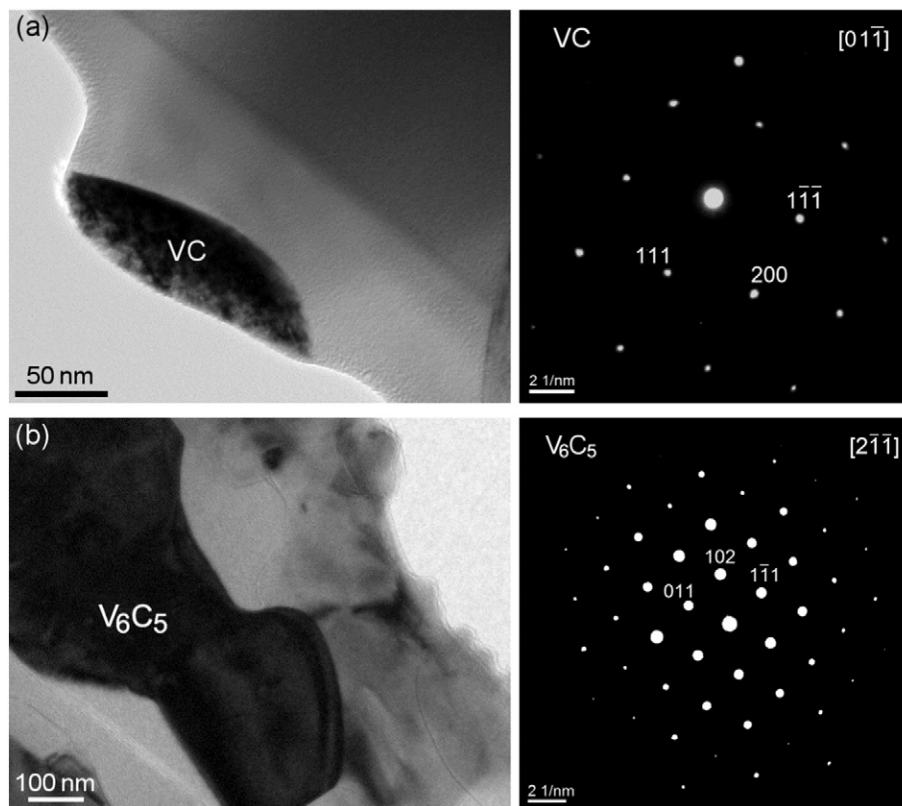


Fig. 7. Cross-sectional TEM image of the upper HVHSS layer showing vanadium carbide formed in the coating and the corresponding selected area diffraction (SAD) patterns: (a) [011] VC (PDF:065-7885); (b) [211] V_6C_5 carbide (PDF: 080-2287).

alloyed layer. More details about the PTA apparatus are described in elsewhere [3].

After PTA modification, transverse cross-sections (marked by a rectangle in Fig. 3(a)) were cut from the surface-alloyed samples by electrical discharge machining. Specimens were subsequently mounted, ground, polished sequentially and then etched by 4 vol.% nital solution. The microstructure was first examined with an optical microscope (OM). Further microscopy and compositional analyses were performed using a Philips XL30-FEG E-SEM and FEI Quanta 200 scanning electron microscope (SEM) equipped with energy dispersive spectrometer (EDS) and JEOL 2010-FEG transmission electron microscope (TEM). The phases presented in the PTA alloyed layer were examined by a PANalytical X'Pert PRO X-ray diffractometer (XRD) using $\text{CuK}\alpha$ radiation. Moreover, X-ray fluorescence (XRF) was used to examine the superficial alloying elements of the samples. The microhardness of transverse sections across the depth was measured using a TMVS-1 Vickers microhardness tester with a load of 200 g and a dwell time of 15 s. The average value of macro-hardness was taken from six measurements evaluated by an HR-150A type Rockwell hardness tester. Dry sliding wear tests were carried out on a standard MG 2000B pin-on-disk tester (made by Xuanhua Testing Machine Factory, China). The dimensions of the sample pins were 6 mm in diameter and 12 mm in height. The rotating disk (GCr15 bearing steel, hardness of 60 ± 1.5 HRC) with a diameter of 70 mm was used as the counter-body. All the wear tests were performed with a sliding time of 10 min at a fixed linear velocity of 0.75 m/s and normal load of 100 N, 150 N, 200 N, 250 N, respectively. The DI substrate, PTA-remelted DI sample and known wear-resistant Mn13 tool steel were also tested for comparisons. The wear mass loss of the specimens was calculated from the weight change after each test weighed by a METTLER TOLEDO analytical balance with

a weight accuracy of 0.1 mg. After the tests, the wear tracks were analyzed by SEM.

3. Results and discussion

3.1. Microstructure evolution

Fig. 3(a) shows the optical macrograph (OM) of a PTA-treated sample. The surface of overlapped large area HVHSS coating is continuous, relatively smooth and flat. There is no visible crack or porosity except few small pores (indicated with circles) in the overlapping areas at the end of every two scanning tracks because the long residence time at the turning points of PTA scans causes excessive thermal accumulation. It can be initially inferred that a hard alloyed layer on the DI substrate was successfully fabricated with proofs supported by the superficial metallic color and the XRF analysis result showing high content of vanadium in the PTA alloyed surface layer (Fig. 3(b)).

Fig. 4(a) and Fig. 5 are cross-sectional backscattered electron SEM micrographs of the specimen showing microstructural evolutions along the depth from the surface. The surface modified layer can be roughly divided into three regions as shown in Fig. 4(a): (1) the top alloyed zone (TAZ), (2) the intermediate remelted zone (IRZ) and (3) the heat-affected zone (HAZ). Besides, between the TAZ and the IRZ there is also a narrow transition zone (TZ) (refer to Fig. 5(b)) where a gradual transition occurs from the growth of dendrites in the IRZ to the formation of fine carbide particles, indicating a good metallurgical bonding between the TAZ and the IRZ zones. The three distinct zones exhibited in the cross-section are because the plasma beam melts simultaneously the pre-placed powder and the substrate surface, and the enrichment of alloying elements decreases in the melt pool

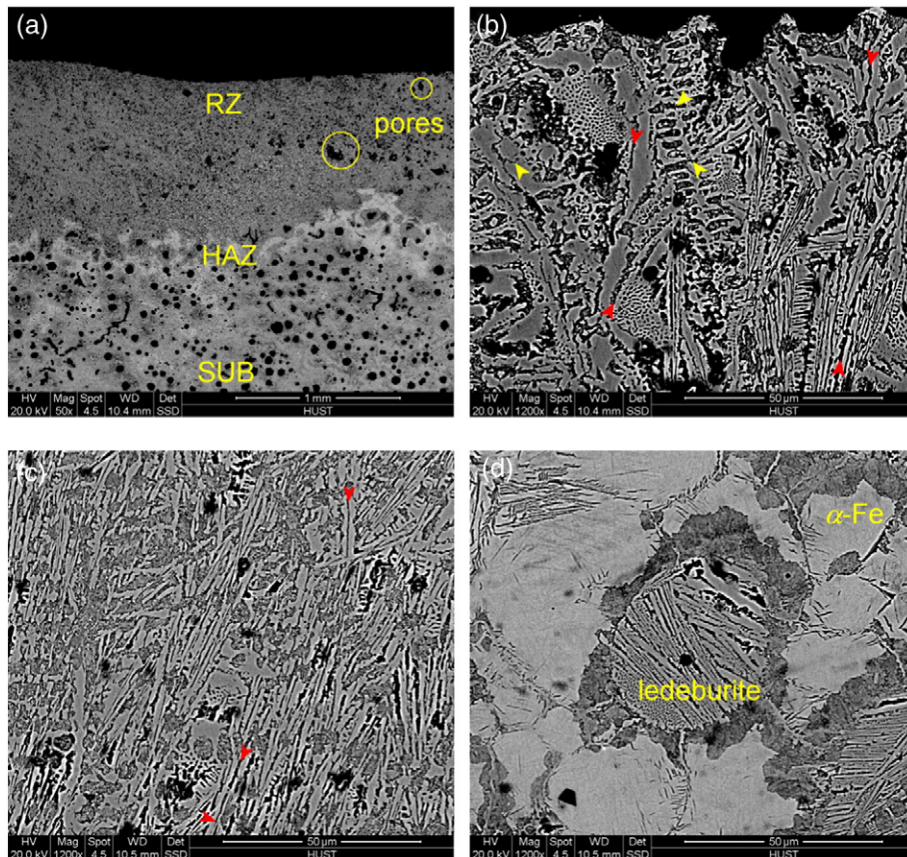


Fig. 8. Microstructural evolutions of PTA remelted sample (90 A, 400 mm/min): (a) cross-section overview; (b) the upper remelted zone (URZ); (c) the bottom remelted zone (BRZ); (d) the heat affected zone (HAZ) [3]. (Note: red and yellow arrows refer to intergranular fracture and transcrystalline fracture, respectively).

along the depth direction. The alloying elements are dissolved into a limited depth and form a thin alloying zone of about 200 μm thick at the near-surface. The alloying composition gradient can be clearly deduced from the EDS line-scan microanalysis (Fig. 4(b)) conducted on the cross-section of the PTA-alloyed HVHSS layer with the scan line indicated in Fig. 4(a). It is interesting to note that the content of V increases gradually from the outer surface until reaching its peak at the base of TAZ and since then levels off, corresponding to the loose distribution of VC particles in the upper TAZ, much denser distribution in the lower TAZ and none in the IRZ, respectively. The content of Fe, however, displays an almost opposite trend with that of V in the TAZ and increases gradually since TZ until reaching its peak in the IRZ. The carbon content remains nearly constant in the TAZ and IRZ. This suggests that the soft graphite nodules, which can be considered as pre-cracks or holes in DI under heavy loading, are effectively dissolved and reacted to form micro-sized spherical carbide particles. This consequently eliminates potential cracking sources [25]. The contents of the rest three alloying elements (Cr, Mo, Ti) remain nearly constant in the TAZ before all drop to almost zero in the IRZ. Notably, the content of vanadium is distinctly higher than that of the other three alloying elements in the TAZ and the gradual decrease of vanadium in the TZ corresponds to the graded microstructure (Fig. 5(b)) that integrates well the TAZ with the IRZ.

As overviewed in Fig. 5(a), a large volume fraction of fine and granular dark particles are uniformly dispersed in the TAZ. The detailed morphology of the dark particles is shown in Fig. 6(a) and 6(b) at higher magnification. These dark particles can be identified mainly as primary MC with the EDS analysis results shown in Table 3 (Spot 3, 4 and 7 in Fig. 6(a, b)). It is noteworthy that all these carbides contain a high content of vanadium and a small amount of chromium, titanium and molybdenum, which implies that the MC have a similar structure to general VC, but in some of the VC vanadium atoms are partly substituted by other alloying atoms to form (V, Cr, Ti, Mo)C [29]. The MC are recognized with TEM analysis as shown in Fig. 7, and the selected area diffraction patterns ascertain two kinds of vanadium carbides, VC and V_6C_5 . Besides, some irregular bright carbides are also observed (refer to Spot 5, 6 in Fig. 6(a) and Spot 9 in Fig. 6(b)). The EDS microanalyses of Spot 5 and Spot 9 suggest these lath-like white areas tend to be molybdenum-containing carbides, probably the $\text{Mo}_2\text{C}/\text{MoC}$ carbides or Mo-Cr eutectic, while the platelike bright areas (Spot 6 in Fig. 6(a)) in the TAZ are likely titanium carbides because of relatively higher content of titanium than other carbides. The microstructural feature of the hardfacing layer is similar to the microstructure of as-cast high-vanadium HSS reported [23,30,31]. However, according to the magnified images of area A (Fig. 6(a)) and area B (Fig. 6(b)) taken from the upper and middle region of the TAZ as indicated in Fig. 5(a), respectively, the carbides observed in the present study are with higher spherical degree and show a denser and more homogeneous distribution with a diameter of $<2\ \mu\text{m}$, which is almost one order of magnitude smaller than that of the as-cast HVHSS. Even in the upper alloyed layer where carbide particles evolved into bulk, cross and blossom shapes due to relatively longer solidification time, the size of the carbide particles is still in the range of submicron to $\sim 5\ \mu\text{m}$. This is because the rapid solidification and high cooling rates prevailing in the PTA process prevent the carbides from excessive growth in the melt. The rough cooling rate referring to Ref. [13] is estimated of a value of 100 $^\circ\text{C}/\text{s}$ for PTA process while only 0.1–5.0 $^\circ\text{C}/\text{s}$ for casting ingots. These characteristics are significant advantages of PTA process compared to the conventional casting techniques. Also note that some wormlike or short rod-like MC eutectic carbides exist with the evidence from the EDS result of Spot 4 taken in Fig. 6(a). In the transition zone shown in Fig. 5(b), some cellular dendrites are visible as well as isolated or partly interconnected bulky carbides rich in chromium (refer to the EDS result of Spot 1 in Fig. 5(b)), which indicates probably the M_7C_3 -type ($\text{M} = \text{Cr}, \text{Fe}$) carbides. Part of the plasma energy is also absorbed by the DI substrate to trigger melting, further yielding a typical characteristic of white cast

iron as shown in Fig. 5(c) and Fig. 6(c) at higher magnification. The IRZ is mainly composed of coarse dendrites and a network of interdendritic eutectic ledeburite and prime lathes of cementite (gray area). These coarse dendrites are characterized by long primary and secondary arms. EDS result of Spot 2 in Fig. 5(c) confirms that the lath carbides only involves Fe and C. Marked dark areas in Fig. 6(c) are former transformed austenite dendrites which are enveloped by the eutectic and have partially transformed to martensite during cooling after the completion of solidification. It is noteworthy that the graphite nodules in the IRZ are nearly completely dissolved and are no longer formed again during solidification. This is because the extremely high cooling rate in the PTA treatment suppresses graphite from nucleation and favors the formation of Fe_3C -type cementite according to the metastable Fe- Fe_3C binary phase diagram [1,2,32]. At the bottom of the IRZ, however, partial dissolution of graphite occurs and some graphite nodules are retained although diminished in diameter. The rapid solidification process also leads to insufficient time for γ -austenite transformation, eventually giving rise to a mixture of modified ledeburite, high carbon needle-like martensite or twinned martensite as well as the residual austenite (tiny light areas segregated by acicular martensite).

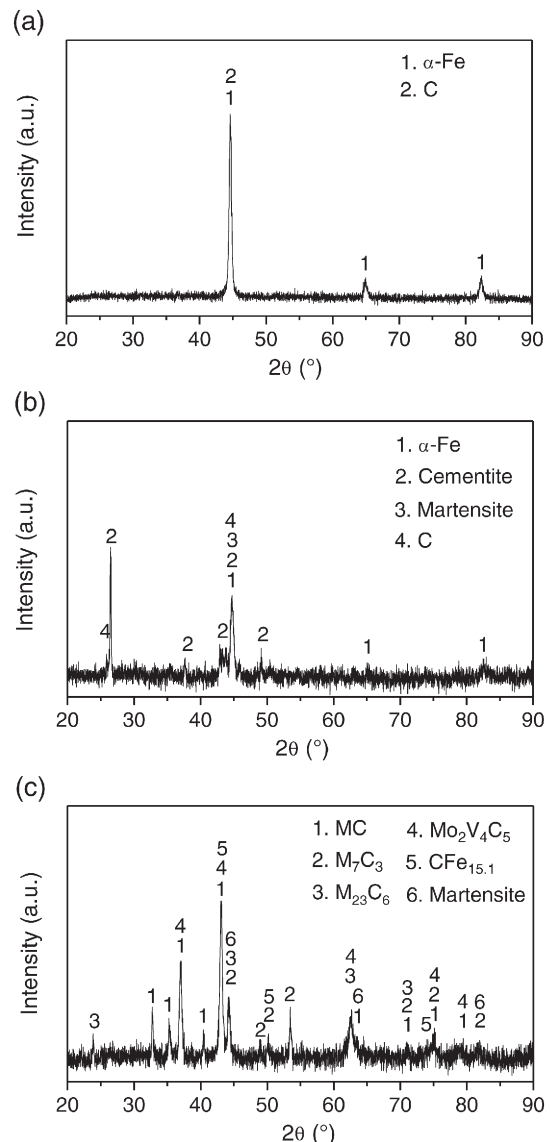


Fig. 9. XRD patterns of (a) DI substrate, (b) PTA-remelted and (c) PTA-alloyed samples.

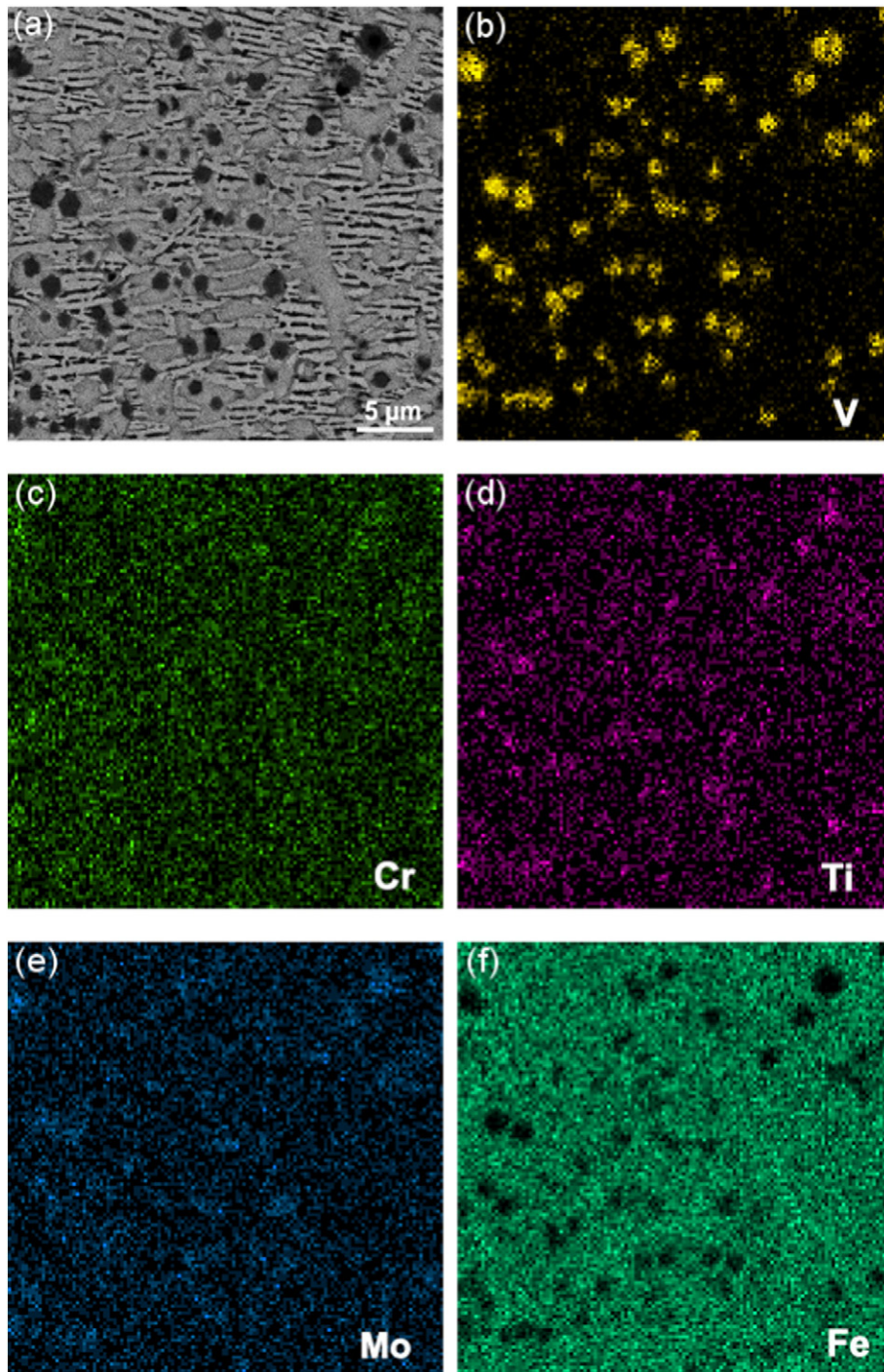


Fig. 10. EDS surface scanning of TAZ: (a) SEM morphology; (b) V element; (c) Cr element; (d) Ti element; (e) Mo element; (f) Fe element.

Table 4
Gibbs free energy of reactions as a function of temperature [36–39].

Reactions	Gibbs energy ΔG^0 (kJ mol ⁻¹)	T (K)
V + C → VC	-102.09 + 0.009581 T	293–2073
7Cr + 3C → Cr ₇ C ₃	-174.401 - 0.0259 T	298–2171
Ti + C → TiC	-186.606 + 0.0132 T	293–2000
Mo + C → MoC	-75.3 - 0.0544 T	298–973
2Mo + C → Mo ₂ C	-45.6 - 0.00418 T	298–1373
3Fe + C → Fe ₃ C	25.958 - 0.02327 T	298–463
	26.711 - 0.02478 T	463–1115
	10.360 - 0.01017 T	1155–1808

The microstructure of PTA remelted DI is presented in Fig. 8 for comparison. Unlike the intercellular eutectic ledeburite as shown in Fig. 5(c), Fig. 8(b) and 8(c) indicate the predominance of primary laths of cementite together with a partial ledeburite structure containing fine pearlite. Sohi et al. [8] described that high solidification rate resulted in positive carbon segregation of zones between austenite dendrites, which transformed the melt into hypereutectic compositions that led to the formation of primary cementite laths. From Fig. 6(d) and Fig. 8(d), it is also seen that the HAZ in alloyed sample has much higher amounts of martensite, and this is because the addition of alloy elements extremely increases the hardenability

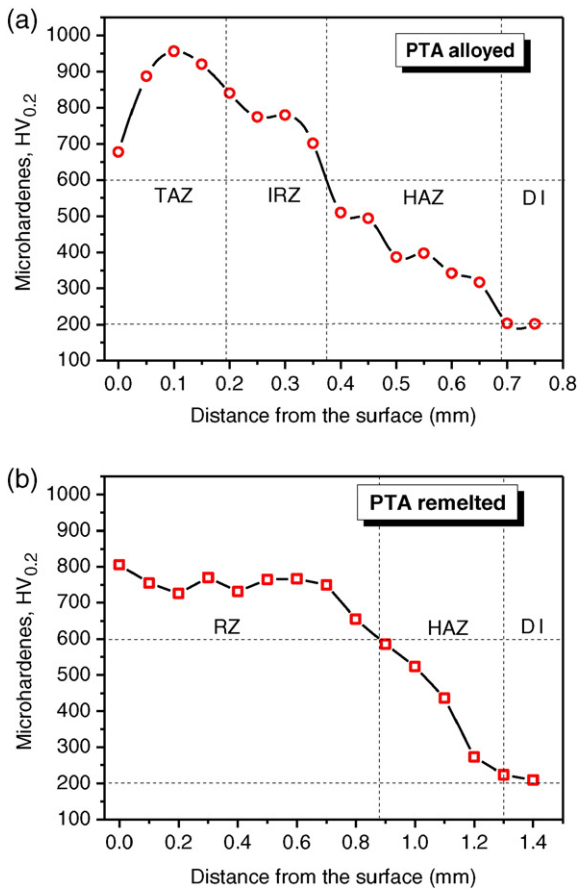


Fig. 11. Microhardness profile of PTA-modified samples as a function of the depth: (a) PTA alloyed and (b) PTA remelted.

and lowers the martensite starting (M_s) temperature. Also, it has been stated by Durand-Charre [33] that the vanadium carbide has higher solubility product, accordingly, austenite can contain a greater amount of carbon with the presence of vanadium, which promotes martensite formation in that martensite (over-saturated solid solution of carbon) generally requires certain amounts of carbon in solution in the austenite.

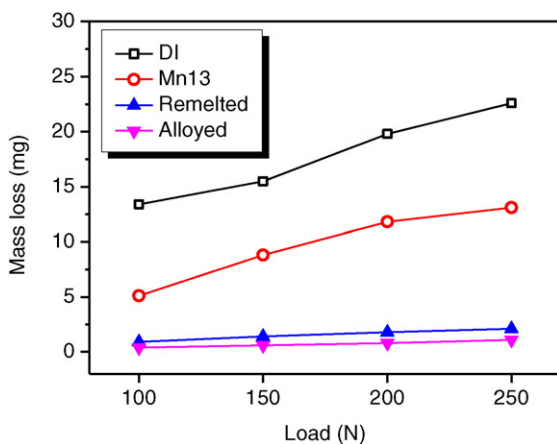


Fig. 12. Weight loss of different samples as a function of normal load in tribo-tests of the same condition (sliding for 10 min).

3.2. Phases and composition distribution

The X-ray diffraction patterns of the untreated DI substrate, PTA-remelted and PTA-alloyed are shown in Fig. 9, respectively. It can be evidently seen that the α -Fe (ferrite) dominates in the untreated ductile iron while the PTA-remelted sample shows strong peaks of cementite (Fe_3C) and martensite. In contrast, no diffraction peak of α -Fe (ferrite) is found in the PTA alloyed sample, and instead a large number of diffraction peaks of new phases can be observed. Fig. 9(c) confirms they are mainly metal carbides comprised of VC (PDF 65-7885), V_6C_5 (PDF 080-2287), MoC (PDF 065-3494) (Note: MC_x ($x \leq 1$) carbides are classified as MC). The peaks of Cr_7C_3 (PDF 036-1482) and $Cr_{23}C_6$ (PDF 065-3132) instead of Fe_3C are noticed as the alloying powder contains Cr element that has a stronger affinity with C to form carbides [34]. Besides, the peaks of martensite (PDF 044-1292) and solid solution (e.g. $Mo_2V_4C_5$) are evidenced from the XRD patterns together with the residual austenite ($CFe_{15.1}$). This is in part because V, Cr, Ti, Mo are elements to stabilize austenite and also because the high cooling rate results in insufficient time for complete austenite–martensite transformation. It should be pointed out that there are chances of other complex carbides formation (such as Ti–V–C, Cr–V–C ternary compounds) due to the addition of multiple alloying elements, and to give a confirmatory analysis other advanced characterization techniques such as TEM and electron backscatter diffraction (EBSD) may be needed.

The EDS area mapping results of V–Cr–Ti–Mo–Fe elements presented in Fig. 10 reveal that the micron-sized dark particles are evidently enriched in vanadium and hence are most likely vanadium carbides (see Fig. 10(b)). In addition, it is clearly seen in Fig. 10(a) that the MC particles serve as pins to interrupt the cementite from large lath-like shape as shown in Fig. 5(c) to short rod-like shape, which is supposed to suppress stress concentration against crack initiation. Therefore, it can be concluded that the microstructure of the TAZ shown in Fig. 10(a) reflects that the PTA-alloyed HVHSS layer have an interrupted ledeburite/cementite matrix rather than ferrite, austenite or tempered martensite matrix commonly observed in the traditional HSS with vanadium [23,29,35].

3.3. Thermodynamics and solidification process

Due to the presence of V, Cr, Ti and Mo, possible reactions between V–C, Cr–C, Ti–C, Mo–C and Fe–C should be considered in the HVHSS system. The different reaction equations accompanied by their respective free energy variations are summarized in Table 4 referring to the published literatures [36–39]. The value of Gibbs free energy ΔG^0 for M–C ($M = V, Cr, Ti, Mo$) reactions are found to be negative, therefore, according to the thermodynamics, the M–C reactions can thermodynamically occur prior to the formation of Fe_3C ($\Delta G^0 > 0$). Notably, the coefficient for MC is very low (0.009581 for V and 0.0132 for Ti), which indicates the carbides are stable and the free energy of formation does not change significantly with temperature. It should be noted that the rapid heating and cooling cause nonequilibrium solidification in the molten pool, thereby promoting the formation of refined and uniformly dispersed MC particles. Furthermore, the formed tiny MC particles become the favored heterogeneous nuclei for the formation of the primary austenite phase [39,40], and thereafter $L \rightarrow (\gamma-Fe + MC)$ eutectic reaction occurs when the melt arrives at the eutectic composition and temperature. The unceasing formation of eutectic MC (the ultrafine rod-like and worm-like carbides shown in Fig. 6(a)) takes place with V depletion and also decomposition of residual interdendritic liquid. Accordingly, this could increase the relative content of Cr and Mo, and eventually leading to the $L \rightarrow (\gamma-Fe + M_7C_3 + M_{23}C_6 + M_2C)$ eutectic reactions [14]. In particular, chromium carbides are finally formed due to its lower melting point (1520–1780 °C) compared with other alloy carbides. However, the Gibbs free energy associated with the other carbides is less negative than that of Cr_7C_3 and as such their formation is less favored thermodynamically. Sil’Man [41] showed with thermodynamically calculated Fe–

C–V phase diagram that in cast iron containing >6.5% V and 3.2–3.3% C it could be possible to obtain a structure containing only the binary eutectic austenite and VC. In such case (namely high vanadium content) the stabilization of cementite and transformation from stable Fe–C system to stable Fe–alloyed M_3C would not be reflected. This also partially explains why cementite is not found in the PTA alloyed HVHSS layer.

3.4. Microhardness and wear properties

The macro-hardness of the PTA-alloyed surface is about 58.7 HRC, slightly higher than that of the PTA-remelted sample (57.4 HRC). Fig. 11 shows the microhardness profile of the PTA-modified samples across the depth. It can be seen from Fig. 11(a) that the microhardness of the TAZ in HVHSS alloyed sample increases from the outer surface (~680 $HV_{0.2}$) and reaches a maximum value of 950 $HV_{0.2}$ at the middle of the zone, which is nearly 5 times as high as that of the substrate. Therefrom, the microhardness fluctuates within the range of 630 to 820 $HV_{0.2}$ in the IRZ and then gradually decreases in the HAZ to the initial hardness of the substrate, approximately 200 $HV_{0.2}$. This result is consistent with the gradual distribution of V element shown in Fig. 4(b) and verifies the dominant role of VC in enhancing the mechanical properties of the PTA alloyed HVHSS. It should be pointed out that the maximum hardness occurring at the subsurface of the alloyed HVHSS layer was also observed in other alloyed systems [25,42]. Zhao et al. [42] attributed the relatively lower hardness at the outermost part of alloyed HSS layer to the presence of a high fraction of soft austenite because austenite stabilizer elements such as Ti were enriched there. In fact, some retained austenite during sliding, to a certain degree, is beneficial for resistance to abrasion by hard particles. An explanation for this behavior is that the strain-induced martensitic transformation can enhance wear resistance at low impact energies [43]. For comparison, the PTA remelted layer exhibits a microhardness ranged between

580 and 805 $HV_{0.2}$ as shown in Fig. 11(b). It can be further observed that the hardness distribution across the remelted depth is more uniform compared with that of the PTA alloyed sample, and this can be interpreted by the homogeneous microstructure of eutectic ledeburite and cementite. It is worth elaborating that the larger remelting depth in the PTA remelted sample (~0.9 mm shown in Fig. 8(a) and Fig. 11(b)) in comparison with the alloyed one is ascribed to the used lower traveling speed of the plasma torch, which caused a higher energy density for deeper remelting according to the equation: $E = P/(\nu D)$, where E, P, ν and D refers to the energy density, power, torch traveling speed and diameter of the plasm beam, respectively [3,24].

The weight loss of the samples of PTA-alloyed, PTA-remelted, standard Mn13 steel and DI substrate respectively under dry sliding tests are illustrated in Fig. 12. The PTA-alloyed and remelted samples experience little changes in weight loss as the normal load increases from 100 N to 250 N. Especially the PTA-alloyed sample loses only 0.4 mg to 1.1 mg with increasing the normal load from 100 N to 250 N, and in comparison, the wear loss of the PTA-remelted sample is 0.9 mg to 2.1 mg. In contrast, the DI has suffered the greatest weight loss from 13.4 mg to 22.6 mg correspondingly, which are >20 times higher compared to the weight loss of the PTA-alloyed samples. As can be seen, the Mn13 sample is also inferior to the PTA-treated samples whether by alloying or remelting in terms of wear resistance to mass removal. Further details can be deduced from the worn surfaces revealed in Fig. 13. The PTA-alloyed sample has an extremely smooth and compact morphology with only slight scratches, suggesting that the HVHSS layer is inherently hard yet tough. This is primarily attributed to the large amount of reinforcing carbides particles (MC , M_7C_3 , $M_{23}C_6$) that act as obstacle against abrasive and adhesive wear as shown in Fig. 13(a). Another contributing factor is that the refined globular particles may lead to low brittleness and suppress crack propagation. It is well-known that the ductile iron is far superior in toughness to gray cast iron,

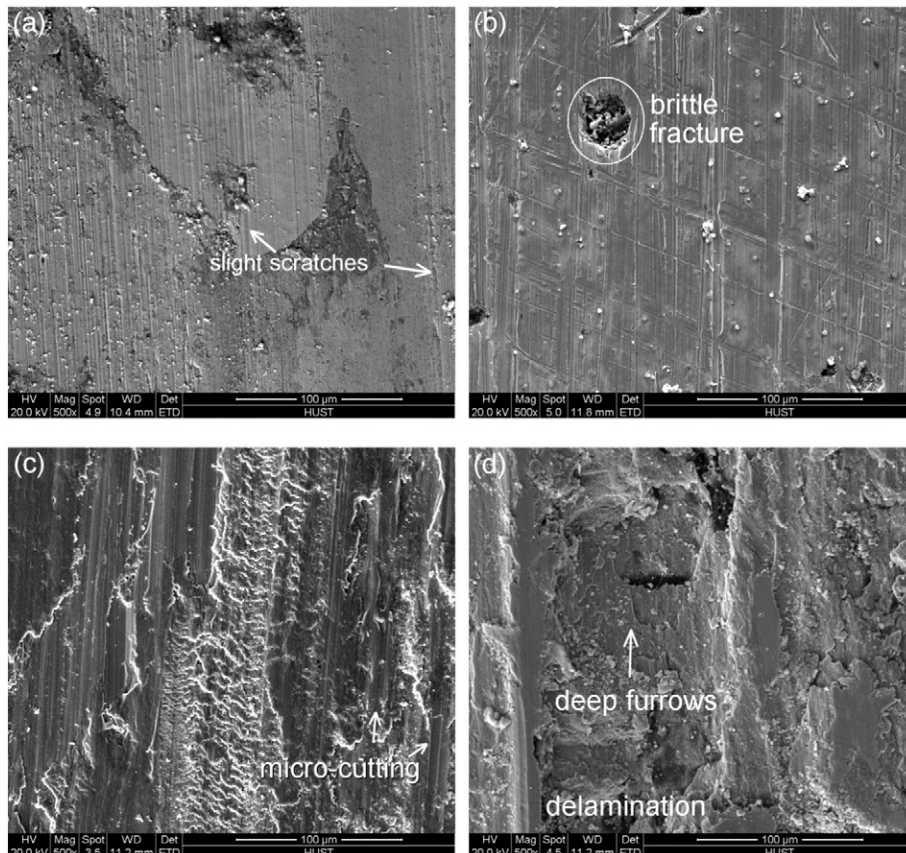


Fig. 13. Secondary electron SEM images showing wear morphologies of different samples (200 N): (a) PTA-alloyed; (b) PTA-remelted; (c) Mn13 steel; (d) DI substrate.

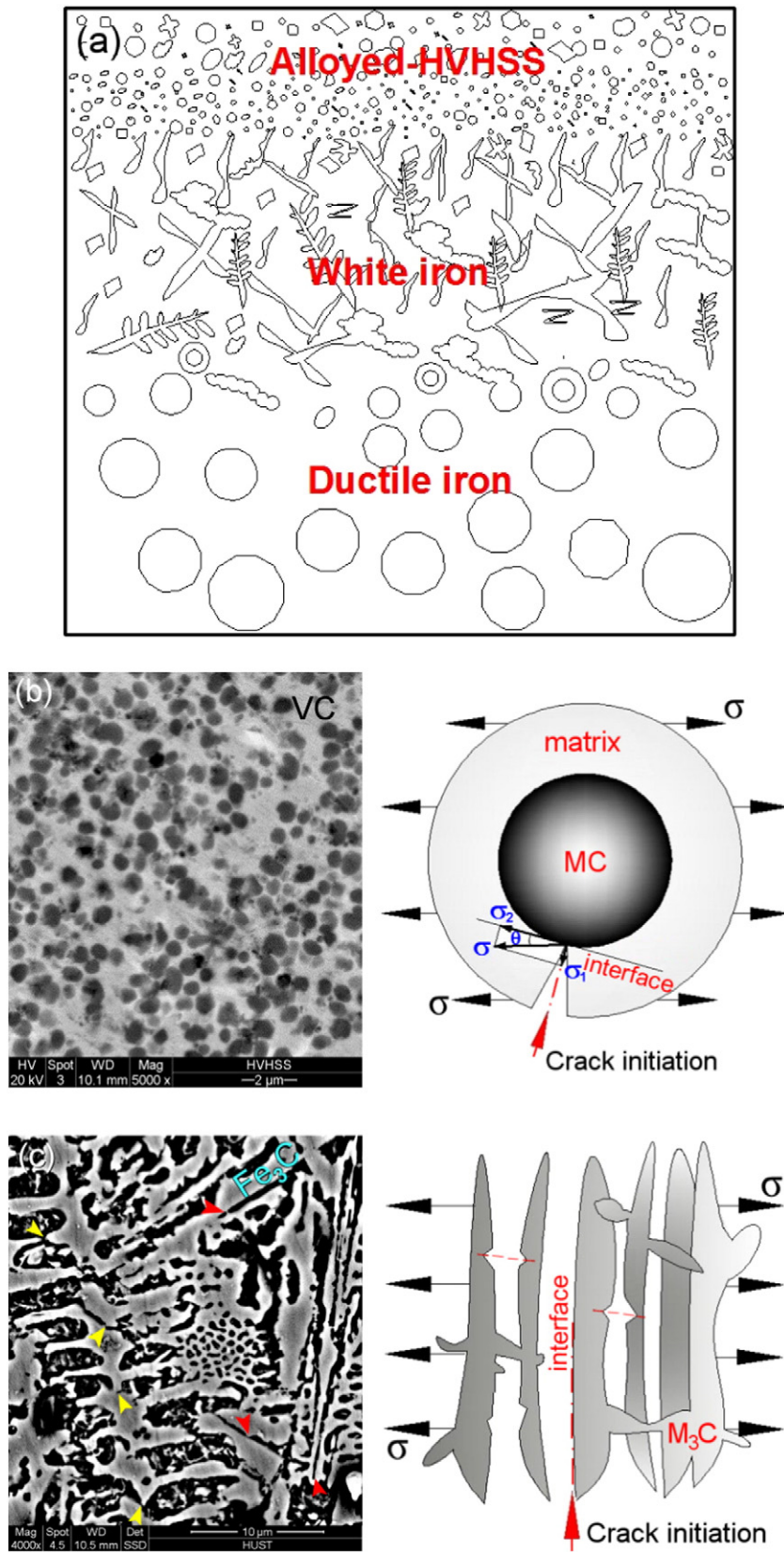


Fig. 14. (a) Schematic of graded material model of PTA-alloyed HVHSS. Crack propagation at the interfaces between two types of carbides and matrix; (b) MC-type spherical reinforcement in PTA-alloyed HVHSS (deflected crack propagation); (c) M_3C -type plate-like reinforcement in PTA-remelted white iron (linear crack propagation and transcrystalline fracture).

because the nodular graphite generates much less fragmentation to the matrix than the flake-like graphite in gray iron does. It is considered that the much finer and spherical MC particles replacing large graphite nodules should contribute to ever higher toughness. Furthermore, the hard IRZ at the subsurface can better support the TAZ to bear higher loads and thus protect the substrate from severe wear by wear mechanisms like fragmentation or micro-fracturing. While the worn surface of PTA-remelted sample is relatively smooth with plastic deformation features as a result of enhanced hardness due to the formation of cementite and ledeburite, the randomly formed craters (see Fig. 13(b)) disclose that the plate-like cementite and cellular ledeburite reinforced hard layer is brittle and more susceptible to spalling and cracking.

The graded HVHSS material model and comparative crack propagation mechanisms for PTA-alloyed and remelted samples are described in Fig. 14. Stress concentration may occur readily at the carbide-matrix interface due to the large hardness differences between the carbides and matrix causing an uneven stress field. Less energy is required for intergranular cracks to propagate through the interfaces than through the matrix; therefore the interfaces become preferential pathways for crack propagation. It is reasonable to assume that cracks become hindered when encountering the hard MC particles as a result of the strong M-C bonding force within a face-centered cubic structure where some C atoms are located at octahedral interstices formed by M ($M = V, Ti, Mo$ and Fe) atoms [44]. Thus the crack tip deviates from the original propagating direction to the direction along the arc interface as shown in Fig. 14(b). The initial main stress σ under the sliding tests can be resolved into σ_1 (normal) and σ_2 (tangential), and only the normal stress component σ_1 effectively acts on deflecting crack propagation direction [25,44,45]. The related stress formulas are shown in Eq. (1) and (2) for cracking towards a spherical carbide particle and along a cementite lath, respectively, where θ is the included angle between the direction of crack propagation and the direction of initial main stress:

$$\sigma_{MC} = \sigma_1 = \sigma \cdot \sin(\theta) \quad (1)$$

$$\sigma_{M_3C} = \sigma \quad (2)$$

It is shown that the driving force for crack propagation at spheroidal MC/matrix interface gradually becomes smaller with decreasing θ as a crack propagates ($\sin(\theta) < 1$). Shi et al. [25] also proposed that frequent deflections prolong the propagating route which consumes more absorbed energy and resistance to crack propagation is thereby increased. It then can be concluded that crack blunting occurs when it propagates to spherical surface of MC particles, ultimately retarding propagation rate or even ceasing crack propagation. In contrast, the stress is intact when a crack propagates along a cementite lath because its platelike shape causes hardly crack deflection (linear propagation) as indicated by red arrows in Fig. 8(b, c) and Fig. 14(c). Besides, the concentration of residual stresses may easily occur at the sharp corners of the intercellular carbides, thereby engendering crack origins and consequently fractures. What is even worse for the white iron is that transcrystalline fractures, which are marked by yellow arrows in Fig. 8(b) and Fig. 14(c), take place easily at the weaker parts of coarse dendrites due to the relatively lower hardness of Fe_3C (HV 980–1110) compared with that of VC (HV 2600–3000) [45,46].

As for the Mn13 sample comprised of single austenite, though having excellent toughness, the lack of hard reinforcement and possibly insufficient sliding pressure to induce work-hardening make it unable to resist the shear forces from the counterpart [47], which is the reason why the micro-cutting and lots of adhesive characteristics are observed in Fig. 13(c). A comparison of the PTA-modified samples and untreated substrate reveals that the DI substrate exhibits loose rippled surface topography with enormous adhesive chippings and serious ploughing grooves. The deep pits and wide furrows formed on the wear surface illustrate that large areas of bulk material are worn off because of its low hardness since the DI consists mainly of soft ferrite and graphite.

4. Conclusions

- (1) A graded HVHSS-white iron coating on ductile iron substrate was produced by PTA alloying process. The alloyed layer has the microstructure primarily comprised of spheroidal V-rich MC particles with size smaller than 5 μm .
- (2) Globular MC particles combined with multiple hard phases such as M_7C_3 , $M_{23}C_6$ and martensite dispersed in a ledeburite matrix make the PTA-alloyed HVHSS material hard yet tough, less susceptible to cracking compared with lathy cementite dominated white iron obtained by PTA remelting.
- (3) Wear tests show excellent tribological performance of the PTA-alloyed HVHSS layer. The hard carbides particles act as obstacle against abrasion and adhesive wear. The PTA-alloyed HVHSS layer provides a superior solution for improving the wear resistance of ductile iron.

Acknowledgments

This work was financially supported by the Key Project of China National Erzhong Group Co. (No. 2012zx04010–081) and the Zhejiang HongMa Foundry Co., Ltd., China. H.T. Cao gratefully acknowledges the Joint PhD Scholarship of China Scholarship Council/University of Groningen.

References

- [1] J.H. Abboud, Microstructure and erosion characteristic of nodular cast iron surface modified by tungsten inert gas, *Mater. Des.* 35 (2012) 677–684.
- [2] M. Shamanian, S.M.R.M. Abarghouie, S.R.M. Pour, Effects of surface alloying on microstructure and wear behavior of ductile iron, *Mater. Des.* 31 (2010) 2760–2766.
- [3] H.T. Cao, X.P. Dong, Q.W. Huang, Z. Pan, J.J. Li, Z.T. Fan, Effect of scanning speed during PTA remelting treatment on the microstructure and wear resistance of nodular cast iron, *Int. J. Miner. Metall. Mater.* 21 (2014) 363–370.
- [4] J. Grum, R. Šturm, Microstructure analysis of nodular iron 400-12 after laser surface melt hardening, *Mater. Charact.* 37 (1996) 81–88.
- [5] K.Y. Benyounis, O.M.A. Fakron, J.H. Abboud, A.G. Olabi, M.J.S. Hashmi, Surface melting of nodular cast iron by Nd-YAG laser and TIG, *J. Mater. Process. Technol.* 170 (2005) 127–132.
- [6] A. Fernández-Vicente, M. Pellizzari, J.L. Arias, Surface melting of nodular cast iron by Nd-YAG laser and TIG, *J. Mater. Process. Technol.* 212 (2012) 989–1002.
- [7] M. Heydarzadeh Sohi, G. Karshenas, S.M.A. Boutorabi, Electron beam surface melting of as cast and austempered ductile irons, *J. Mater. Process. Technol.* 153–154 (2004) 199–202.
- [8] M. Heydarzadeh Sohi, M. Ebrahimi, H.M. Ghasemi, A. Shahripour, Microstructural study of surface melted and chromium surface alloyed ductile iron, *Appl. Surf. Sci.* 258 (2012) 7348–7353.
- [9] A. Amirsadeghi, M.H. Sohi, Comparison of the influence of molybdenum and chromium TIG surface alloying on the microstructure, hardness and wear resistance of ADI, *J. Mater. Process. Technol.* 201 (2008) 673–677.
- [10] J. Grum, R. Šturm, Comparison of measured and calculated thickness of martensite and ledeburite shells around graphite nodules in the hardened layer of nodular iron after laser surface remelting, *Appl. Surf. Sci.* 187 (2002) 116–123.
- [11] X.B. Wang, C.G. Li, X.M. Peng, L.B. Shi, Z. Zhang, The powder's thermal behavior on the surface of the melting pool during PTA powder surfacing, *Surf. Coat. Technol.* 201 (2006) 2648–2654.
- [12] M. Godec, B.Š. Batič, D. Mandrino, A. Nagode, V. Leskovšek, S.D. Škapin, M. Jenko, Characterization of the carbides and the martensite phase in powder-metallurgy high-speed steel, *Mater. Charact.* 61 (2010) 452–458.
- [13] L. Bourithis, G.D. Papadimitriou, Synthesizing a class "M" high speed steel on the surface of a plain steel using the plasma transferred arc (PTA) alloying technique: microstructure and wear properties, *Mater. Sci. Eng. A* 361 (2003) 165–172.
- [14] K.C. Hwang, S. Lee, H.C. Lee, Effects of alloying elements on microstructure and fracture properties of cast high speed steel rolls: Part I: microstructural analysis, *Mater. Sci. Eng. A* 254 (1998) 282–295.
- [15] C. Navas, A. Conde, B.J. Fernández, F. Zubiri, J. de Damborenea, Laser coatings to improve wear resistance of mould steel, *Surf. Coat. Technol.* 194 (2005) 136–142.
- [16] G.F. Sun, K. Wang, R. Zhou, A.X. Feng, W. Zhang, Effect of different heat-treatment temperatures on the laser clad M3:2 high-speed steel, *Mater. Des.* 65 (2015) 606–616.
- [17] A.S. Chaus, Microstructural and properties evaluation of M2 high speed steel after inoculating addition of powder W and WC, *Mater. Sci. Technol.* 30 (2014) 1105–1115.
- [18] V. Lazić, D. Milosavljević, S. Aleksandrović, P. Marinković, G. Bogdanović, B. Nedeljković, Carbide type influence on tribological properties of hard faced steel layer part I - theoretical considerations, *Tribol Ind* 32 (2) (2010) 11–20.

- [19] N Axén, K.H. Zum Gahr, Abrasive wear of TiC-steel composite clad layers on tool steel. *Wear* 157 (1992) 189–201.
- [20] L.J. Xu, J.D. Xing, S.Z. Wei, Y.Z. Zhang, R. Long, Optimisation of chemical composition of high speed steel with high vanadium content for abrasive wear using an artificial neural network, *Mater. Des.* 28 (2007) 1031–1037.
- [21] S.Z. Wei, J.H. Zhu, L.J. Xu, Research on wear resistance of high speed steel with high vanadium content, *Mater. Sci. Eng. A* 404 (2005) 138–145.
- [22] L.J. Xu, S.Z. Wei, J.D. Xing, R. Long, Effects of carbon content and sliding ratio on wear behavior of high-vanadium high-speed steel (HVHSS) under high-stress rolling-sliding contact, *Tribol. Int.* 70 (2014) 34–41.
- [23] S.Z. Wei, J.H. Zhu, L.J. Xu, R. Long, Effects of carbon on microstructures and properties of high vanadium high-speed steel, *Mater. Des.* 27 (2006) 58–63.
- [24] M.B. Karamiş, K. Yıldızlı, Surface modification of nodular cast iron: a comparative study on graphite elimination, *Mater. Sci. Eng. A* 527 (2010) 5225–5229.
- [25] K.Y. Shi, S.B. Hu, H.F. Zheng, Microstructure and fatigue properties of plasma transferred arc alloying TiC-W-Cr on gray cast iron, *Surf. Coat. Technol.* 206 (2011) 1211–1217.
- [26] Q.Y. Hou, Influence of molybdenum on the microstructure and properties of a FeCrBSi alloy coating deposited by plasma transferred arc hardfacing, *Surf. Coat. Technol.* 225 (2013) 11–20.
- [27] S. Ozel, B. Kurt, I. Somunkiran, N. Orhan, Microstructural characteristic of NiTi coating on stainless steel by plasma transferred arc process, *Surf. Coat. Technol.* 202 (2008) 3633–3637.
- [28] R. Veinthal, F. Sergejev, A. Zikin, R. Tarbe, J. Hornung, Abrasive impact wear and surface fatigue wear behaviour of Fe-Cr-C PTA overlays, *Wear* 301 (2013) 102–108.
- [29] C. Kim, Y. Kim, J. Park, S. Lee, N. Kim, J. Yang, Effects of alloying elements on microstructure, hardness, and fracture toughness of centrifugally cast high-speed steel rolls, *Metall. Mater. Trans. A* 36 (2005) 87–97.
- [30] L.J. Xu, J.D. Xing, S.Z. Wei, Y.Z. Zhang, R. Long, Study on relative wear resistance and wear stability of high-speed steel with high vanadium content, *Wear* 262 (2007) 253–261.
- [31] Y.P. Ji, S.J. Wu, L.J. Xu, Y. Li, S.Z. Wei, Effect of carbon contents on dry sliding wear behavior of high vanadium high speed steel, *Wear* 294–295 (2012) 239–245.
- [32] K.F. Alabeedi, J.H. Abboud, K.Y. Benyounis, Microstructure and erosion resistance enhancement of nodular cast iron by laser melting, *Wear* 266 (2009) 925–933.
- [33] M. Durand-Charre, *Microstructure of Steels and Cast Irons*, Springer, New York, 2004.
- [34] X. Tong, M.J. Dai, Z.H. Zhang, Thermal fatigue resistance of H13 steel treated by selective laser surface melting and CrNi alloying, *Appl. Surf. Sci.* 271 (2013) 373–380.
- [35] V. Vitry, S. Nardone, J.P. Breyer, M. Sinnaeve, F. Delaunoy, Microstructure of two centrifugal cast high speed steels for hot strip mills applications, *Mater. Des.* 34 (2012) 372–378.
- [36] X.H. Wang, F. Han, S.Y. Qu, Z.D. Zou, Microstructure of the Fe-based hardfacing layers reinforced by TiC-VC-Mo₂C particles, *Surf. Coat. Technol.* 202 (2008) 1502–1509.
- [37] Q.L. Wu, W.G. Li, N. Zhong, W. Gang, W. Haishan, Microstructure and wear behavior of laser cladding VC-Cr₇C₃ ceramic coating on steel substrate, *Mater. Des.* 49 (2013) 10–18.
- [38] A. Agarwal, N.B. Dahotre, Pulsed electrode surfacing of steel with TiC coating: microstructure and wear properties, *J. Mater. Eng. Perform.* 8 (1999) 479–486.
- [39] F.J. Cheng, Y.S. Wang, T.G. Yang, Microstructure and wear properties of Fe-VC-Cr₇C₃ composite coating on surface of cast steel, *Mater. Charact.* 59 (2008) 488–492.
- [40] H. Zhang, Y. Zou, Z.D. Zou, D.T. Wu, Microstructure and properties of Fe-based composite coating by laser cladding Fe-Ti-V-Cr-CeO₂ powder, *Opt. Laser Technol.* 65 (2015) 119–125.
- [41] G.I. Sil'man, Phase diagram of the Fe-C-V system and its application to metallography of steels and cast irons, *Met. Sci. Heat Treat.* 34 (1992) 665–670.
- [42] H. Zhao, J.J. Li, Z.Z. Zheng, A.H. Wang, Q.W. Huang, D.W. Zeng, Microstructure and high-temperature wear properties of in situ TiC composite coatings by plasma transferred arc surface alloying on gray cast iron, *Int. J. Miner. Metall. Mater.* 22 (2015) 1273–1282.
- [43] I.M. Hutchings, *Tribology: Friction and Wear of Engineering Materials*, Edward Arnold, London, 1992.
- [44] M.J. Wang, Y.M. Li, Z.X. Wang, E. Bao, Effect of rare earth elements on the thermal cracking resistance of high speed steel rolls, *J. Rare Earths* 29 (2011) 489–493.
- [45] L.J. Xu, J.D. Xing, S.Z. Wei, Y.Z. Zhang, R. Long, Investigation on wear behaviors of high-vanadium high-speed steel compared with high-chromium cast iron under rolling contact condition, *Mater. Sci. Eng. A* 434 (2006) 63–70.
- [46] J.J. Coronado, A. Sinatora, Abrasive wear study of white cast iron with different solidification rates, *Wear* 267 (2009) 2116–2121.
- [47] M. Abbasi, S. Kheirandish, Y. Kharrazi, J. Hejazi, On the comparison of the abrasive wear behavior of aluminum alloyed and standard Hadfield steels, *Wear* 268 (2010) 202–207.